TpBD COF@ZnIn$_2$S$_4$ nanosheets: A novel S-scheme heterojunction with enhanced photoreactivity for hydrogen production

Shutong Bao [a], Qiuyan Tan [b], Shaodan Wang [a], Jie Guo [a], Kangle Lv [b,*], Sónia A.C. Carabineiro [c], Lili Wen [a,*]

[a] Key Laboratory of Pesticide & Chemical Biology of Ministry of Education, College of Chemistry, Central China Normal University, Wuhan 430079, PR China
[b] Key Laboratory of Resources Conversion and Pollution Control of the State Ethnic Affairs Commission, College of Resources and Environment, South-Central Minzu University, Wuhan 430074, PR China
[c] LAQV-REQUIMTE, Department of Chemistry, NOVA School of Science and Technology, Universidade NOVA de Lisboa, Caparica 2829-516, Portugal

ARTICLE INFO

ABSTRACT

Covalent-organic frameworks (COFs) are emerging photocatalysts with porous structures and excellent light-harvesting abilities. However, their photoreactivity still needs further improvement before they can be used in practical applications. Herein, we report, for the first time, on the construction of a heterojunction consisting of core-shell structured 1,3,5-triformylphloroglucinol (Tp) and 4,4′-biphenylenediamine (BD) COF at ZnIn$_2$S$_4$ (ZIS) nanosheets, using a microwave-hydrothermal method. The best performing sample, TpBD COF@ZIS-10 (with a ZIS:TpBD COF mass ratio of 10:1), in the absence of a co-catalyst, achieves a visible-light-driven H$_2$ production rate of 2304 μmol g^{-1} h^{-1} with an AQE of 5.02% at 420 nm, and exhibits excellent stability. The improved photocatalytic performance of TpBD COF@ZIS was attributed to the strong interaction at the interface and the S-scheme charge transfer mechanism, which not only stimulates efficient charge separation and migration, suppressing recombination, but also preserves the higher redox potentials of photo-generated electrons and holes.

1. Introduction

The extensive consumption of fossil fuels leads to critical issues in nowadays society, such as energy crisis and environmental pollution [1–3]. In recent years, one of the effective routes for the mitigation of these problems is the conversion of the unlimited natural solar energy into hydrogen gas using semiconductor-based photocatalytic water splitting [4–6]. Among several common semiconductors, the ternary chalcogenide ZnIn$_2$S$_4$ (ZIS) is a promising reduction photocatalyst, with layered structure, narrow band gap, excellent photostability, low toxicity and facile preparation [7–10]. However, for pristine semiconductors, the contradiction between light absorption and redox potential in thermodynamics presents a significant challenge to achieving efficient and stable H$_2$ production [11]. Fortunately, heterojunction construction provides an effective way to solve the problem, as it facilitates the photogenerated charge migration and separation, resulting in enhanced photocatalytic activity [12–21]. Therefore, some researchers dedicated efforts to strengthening the photocatalytic performance of ZIS by constructing heterojunctions [22–29].

Conventional type-II heterojunctions hinder the photocatalytic oxidation and reduction reactions, as they decrease the redox abilities of photogenerated electron-hole pairs [12]. In contrast, innovative Step-scheme (S-scheme) heterojunctions not only promote the separation of charge carriers, but also preserve the higher redox potentials of electrons and holes, which therefore benefits the photocatalytic redox reactions [30]. For example, Zhang et al. [31] report a TiO$_{2-X}$/Tp-Pa-1-COF S-scheme photocatalyst (where Pa-1 is paraphenylenediamine and TiO$_{2-X}$ is titania mixed with NaBH$_4$ and calcined at 350 ℃), exhibiting a much higher photocatalytic activity towards H$_2$ production than pure TiO$_{2-X}$, due to the optimized redox ability. In order to develop efficient S-scheme heterostructures, the selection of semiconductors with considerable band positions is of great importance, as they act as collectors of the photogenerated electrons and holes.

Covalent-organic frameworks (COFs) are crystalline and porous structures formed by covalent bonding of organic molecules [32,33], acting as emerging photocatalysts for H$_2$ production under visible-light irradiation. COFs have ordered structure, large surface area, low density, tunable band gap and outstanding chemical stability. Most of the

reported COFs have 2D structures due to the strong interaction between neighboring layers [34–36]. The π-π stacking within layers leads to strong electronic interactions, providing an alternative pathway for charge carrier transport, in addition to transfer within the covalent structures [37–39]. In particular, Schiff-based COFs (such as TpBD COF) show intense colorations, ranging from orange to dark red, which can broaden the range of light absorbed in the visible-light region, leading to an improved light utilization efficiency [40,41]. Thus, COFs-based S-scheme heterojunctions have great potential to enhance photocatalytic activity by promoting an efficient separation of photogenerated charge carriers. However, to the best of our knowledge, the construction of a heterojunction between COFs and ZIS is rarely reported.

Herein, we report the construction of a TpBD COF@ZIS S-scheme heterojunction by in-situ growth of ZIS on the surface of TpBD COF using a facile microwave-hydrothermal method (Scheme 1), which greatly improves the photocatalytic activity of ZIS for efficient water splitting and H_2 production. Under visible-light irradiation ($\lambda > 420$ nm), the optimal TpBD COF@ZIS composite without co-catalyst shows a significantly enhanced H_2 production rate of 2304 μmol g^{-1} h^{-1} with an apparent quantum efficiency (AQE) of 5.02% at 420 nm, which is around 16.3 and 9.8 times higher than the values of pristine TpBD COF and ZIS, respectively. Analysis of in-situ XPS and ESR results, together with DFT calculations reasonably demonstrate the S-scheme charge transfer mechanism between TpBD COF and ZIS, which renders TpBD COF@ZIS excellent photogenerated carriers separation efficiency and high redox potentials of VB holes and CB electrons, respectively. Due to the protection of TpBD COF, the photo-stability of ZIS is greatly improved, indicating the practical applications of this TpBD COF@ZIS S-scheme heterojunction.

2. Experimental

2.1. Synthesis of TpBD COF

1,3,5-triformylphloroglucinol (Tp) was prepared according to the literature [42], and TpBD COF was obtained by a modified reported method [41]. The detailed processes for the synthesis of TpBD COF can be found in Supporting Information.

2.2. Synthesis of $ZnIn_2S_4$ (ZIS)

ZIS was prepared through a microwave-hydrothermal reaction. Firstly, 0.170 g of $ZnCl_2$ (1.25 mmol), 0.733 g $InCl_3 \bullet 4 H_2O$ (2.50 mmol) and 0.375 g thioacetamide (TAA, 5.0 mmol) were added into a flask containing 50 mL of deionized water and stirred for 60 min. The mixture was heated in a microwave-hydrothermal reaction system in a 100 mL Teflon-lined autoclave at 90 ℃ for 30 min, and then at 120 ℃ for 45 min. The resulting precipitates were washed with deionized water and ethanol, and dried at 80 ℃ for 6 h under vacuum to obtain faint yellow powders.

2.3. Synthesis of TpBD COF@ZIS-X composites

Photocatalysts with various mass ratios were synthesized under same reaction conditions. Samples were labelled as TpBD COF@ZIS-X (X = 5, 10 or 15, the mass ratios of ZIS:TpBD COF, that is, 5:1, 10:1 and 15:1). As an example, the detailed synthetic procedure for TpBD COF@ZIS-10 sample is given below: 50 mL of deionized water was used to disperse 52.8 mg of the prepared TpBD COF. After sonication for 10 min, 1.25 mmol of $ZnCl_2$, 2.50 mmol of $InCl_3 \bullet 4 H_2O$, and 5.0 mmol of TAA were added under magnetic stirring. The following procedures, including microwave-hydrothermal reaction and washing, were similar to the synthesis of ZIS.

2.4. Photocatalytic activity measurements

The photocatalytic activity of the photocatalysts was evaluated using water splitting to produce hydrogen gas through an on-line trace gas analysis photoreaction device (Labsolar-6A, Beijing Perfectlight) connected to a gas chromatograph (Nexis GC-2030, Shimadzu). Detailed procedures for photocatalytic hydrogen production and the calculation of AQE can be found in Supporting Information.

3. Results and discussion

3.1. Zeta potential

The results of the zeta potential measurements of TpBD COF and ZIS in deionized water are shown in Fig. 1a. TpBD COF shows a positive zeta potential of 8.57 mV, whereas ZIS exhibits a negative zeta potential of − 34.0 mV under the same conditions. The opposite zeta potentials result in strong electrostatic attraction between TpBD COF and ZIS, which is beneficial for the electron migration between them [43]. Moreover, the Coulomb electrostatic interaction between TpBD COF and
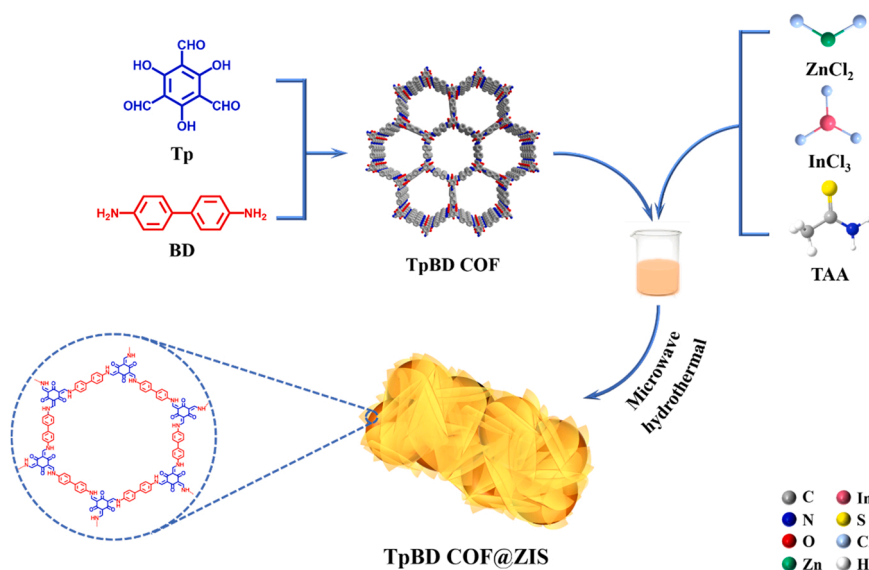
Scheme 1. Synthesis of the TpBD COF@ZIS heterojunction (see Experimental section for details).
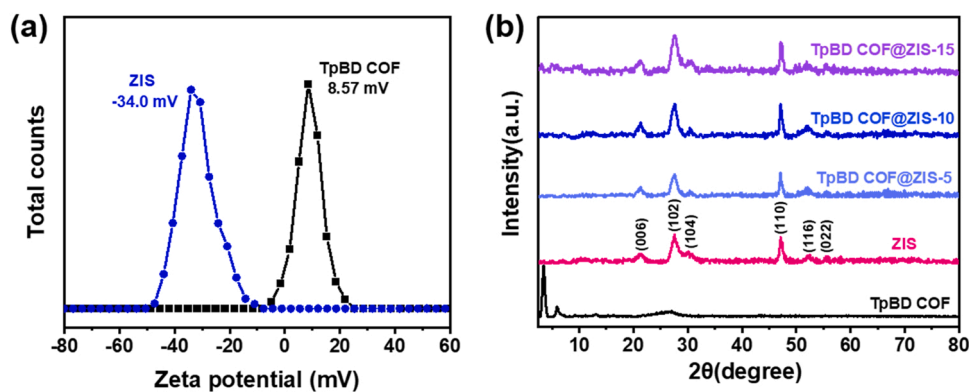
Fig. 1. (a) Zeta potentials of TpBD COF and ZIS in deionized water. (b) XRD patterns of the synthesized photocatalysts.

ZIS leads to the formation of a stable TpBD COF@ZIS heterojunction.

3.2. Structure and morphology characterization

X-ray diffraction (XRD) was conducted to determine the phase structures of the synthesized samples. Fig. 1b shows the XRD patterns of
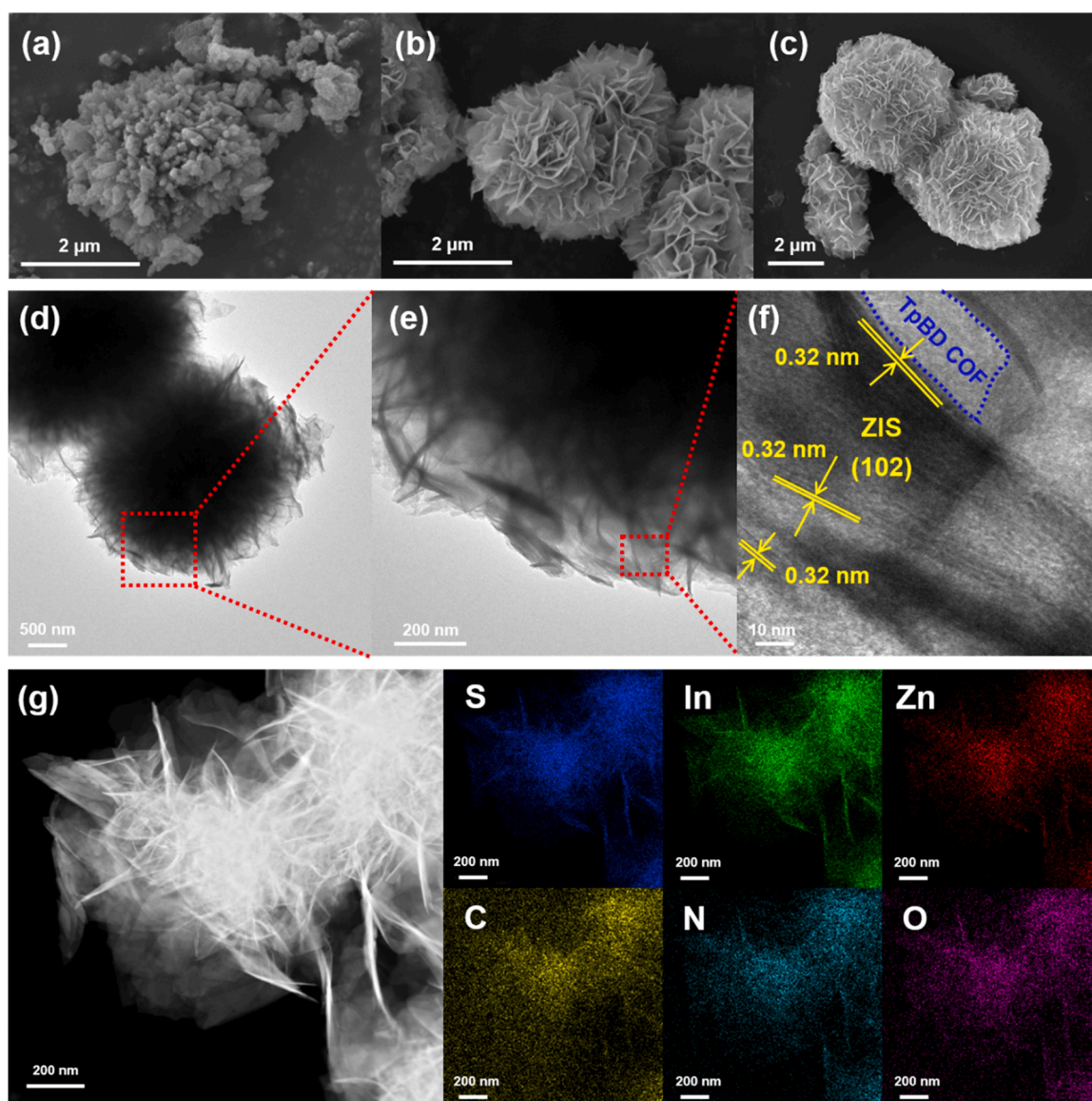

Fig. 2. SEM images of TpBD COF (a) and ZIS nanosheets (b). SEM image (c), TEM images (d-e), HRTEM image (f), HADDF-STEM and EDS elements mapping images (g) of TpBD COF@ZIS-10.

TpBD COF. The diffraction peaks at 3.3, 5.9, and 27.3° can be assigned to the diffractions of the (100), (200), and (001) crystal planes of TpBD COF, respectively [41], indicating the successful synthesis of the material. Concerning ZIS, the diffraction peaks can be indexed to the hexagonal crystal structure (JCPDS NO.65–2023) [44]. No TpBD COF related diffraction peaks were observed in the XRD patterns of TpBD COF@ZIS-X samples, due to the low crystallinity and small amounts of TpBD COF in the composites. To confirm the stability of TpBD COF in this synthesis system, the prepared sample was subjected to the same reaction conditions as TpBD COF@ZIS-X without ZnCl₂, InCl₃·4 H₂O and TAA. The characteristic peaks of TpBD COF were clearly observed in the XRD patterns (Fig. S1), confirming its stability. Fourier transform infrared spectroscopy (FTIR) was carried out to identify the characteristic functional groups of the photocatalysts (Fig. S2). For pure ZIS, the absorption peaks around 1644 and 1414 cm⁻¹, found in all samples, correspond to the surface absorbed water molecules and hydroxyl groups [45]. The peaks of pristine TpBD COF at 1253 and 1612 cm⁻¹ can be attributed to C–N and C=O bonds, respectively [41]. As the reaction of TpBD COF is an irreversible transformation from enol to ketone, C–N bonds become the characteristic feature, which confirms the successful synthesis of TpBD COF. All TpBD COF@ZIS-X samples show the characteristic C–N peaks, indicating that the composite materials are successfully synthesized and that the introduction of ZIS has no influence on the chemical framework of TpBD COF.

The microstructure and morphology of the prepared TpBD COF, ZIS and TpBD COF@ZIS-10 samples are characterized by scanning electron microscopy (SEM) and transmission electron microscopy (TEM). TpBD COF exhibits a block morphology of 2–7 μm in size (Fig. 2a). The SEM images of ZIS show a flower-like hierarchical microsphere consisting of intersecting nanosheets (Fig. 2b), which facilitate the exposure of the active sites. The TpBD COF@ZIS-10 sample clearly exhibits uniformly spread, thin and staggered ZIS nanosheets on the TpBD COF surface (Fig. 2c). TEM and high resolution TEM (HRTEM) confirm this morphology, with clear lattice fringes, having an interplanar spacing of 0.32 nm, being ascribed to the (102) crystal plane of hexagonal ZIS (Fig. 2d-f and Fig. S3c) [46]. The contact interface between TpBD COF and ZIS is marked by a blue dashed line (Fig. 2f). Additionally, SEM and TEM images of TpBD COF@ZIS-10 do not show the presence of TpBD COF, demonstrating that TpBD COF and ZIS nanosheets are well combined and not in the form of a physical mixture. The chemical composition and element distribution of TpBD COF@ZIS-10 are revealed by HAADF-STEM and energy dispersive X-ray spectroscopy (EDS) elements mapping in Fig. 2g. These images clearly show the homogeneous spatial distribution of S, In, Zn, C, N and O, further validating the formation of the TpBD COF@ZIS heterojunction. In addition, the EDS spectrum of TpBD@ZIS-10 (Fig. S4) shows that the atomic ratio of Zn, In and S is about 1:2:4, which is well consistent with the composition of ZnIn₂S₄.

The TpBD COF, ZIS and TpBD COF@ZIS-X composites were also characterized by N₂ adsorption (Figs. S5a–b). TpBD COF displays a typical microporous structure with a type I isotherm, without hysteresis. ZIS shows a type IV isotherm with a hysteresis loop (H3 type), while TpBD COF@ZIS-X composites exhibit a type IV isotherm with large hysteresis between adsorption and desorption branches. The pore size distribution confirms the presence of both micropores and mesopores (Fig. S5b). The surface area and pore volume of ZIS are 74.20 m²g⁻¹ and 0.17 cm³g⁻¹, respectively. For TpBD COF, the corresponding values are 528.8 m²g⁻¹ and 0.28 cm³g⁻¹. The surface area and pore volume of TpBD COF@ZIS-10 are 117.5 m²g⁻¹ and 0.20 cm³g⁻¹, TpBD COF has the largest surface area and pore volume, effectively inhibiting the agglomeration of ZIS nanosheets and providing more catalytically active sites for substrate adsorption.

3.3. XPS analysis

In order to determine surface species and chemical interactions in the TpBD COF@ZIS heterojunction, XPS measurements were acquired for TpBD COF, ZIS and TpBD COF@ZIS-10 samples. The XPS survey spectrum in Fig. 3a, shows the presence of C, N, O, Zn, In and S elements in the TpBD COF@ZIS-10 composite. The deconvolution results of C 1 *s*, N 1 *s*, Zn 2*p*, In 3*d* and S 2*p* spectra of TpBD COF@ZIS-10, obtained in the dark and with illumination by a 420 nm Xenon arc lamp light (TpBD COF@ZIS-10 light) are shown in Fig. 3b-f. As displayed in Fig. 3b, the C 1 *s* spectra of all samples can be deconvoluted into three carbon species of sp² C–C (284.7 eV), C–N (286.0 eV), and C=O bonds (288.9 eV), respectively. The N 1 *s* XPS spectra (Fig. 3c) show one peak, matching the C–NH–C (399.9 eV) of TpBD COF [47,48]. For Zn 2*p*, the peaks located at 1022.1 and 1045.2 eV are attributed to Zn 2$p_{3/2}$ and 2$p_{1/2}$ orbitals, respectively (Fig. 3d). The binding energy difference of about 23.1 eV further confirms the presence of Zn²⁺ in ZIS. The two deconvoluted peaks in Fig. 3e can be attributed to the 3$d_{5/2}$ (444.8 eV) and 3$d_{3/2}$ (452.4 eV) of In 3*d* with + 3 valence state, respectively. The peaks centered at 161.6 and 162.6 eV in Fig. 3f are assigned to 2$p_{3/2}$ and 2$p_{1/2}$ of S 2*p* respectively, being characteristic of S²⁻ and in agreement with literature [46,49].

The binding energy of the electrons of an atom is determined by the strong Coulomb attraction between the outer electrons and nucleus. Therefore, changes in the binding energy of elements can significantly impact the atom electron density. For example, a decrease in electron density corresponds to an increase of binding energy and vice versa. This is often used to study the transfer of electrons in hybridized photocatalysts. The changes in binding energy before and after the formation of a heterojunction are often used to determine the direction of the electron transfer in the hybridized photocatalyst system [50,51].

Concerning the illuminated TpBD COF@ZIS-10 sample, the binding energies of C 1 *s* and N 1 *s* are upshifted under light irradiation, compared to the values obtained in the absence of light (Fig. 3b-c). In contrast, the binding energies of Zn 2*p*, In 3*d* and S 2*p* in TpBD COF@ZIS-10 light sample are negatively shifted, in comparison with those obtained in the dark (Fig. 3d-f). Compared to pure TpBD COF, the binding energies of C 1 *s* and N 1 *s* in the TpBD COF@ZIS-10 composite are clearly shifted towards lower energy levels in the dark (Fig. 3b-c), indicating an increase in the electron density of TpBD COF. In contrast, compared to pure ZIS, the binding energies of Zn 2*p*, In 3*d*, and S 2*p* in TpBD COF@ZIS-10 composite are significantly shifted towards higher energy levels in the dark (Fig. 3d-f), indicating a decrease in the electron density of ZIS. These results suggest that, in the absence of light, electrons tend to migrate from ZIS to TpBD COF, due to the intimate interface contacts. This electron migration between ZIS and TpBD COF leads to the production of an interfacial electric field (IEF) in the TpBD COF@ZIS heterojunction [31,52].

3.4. Optical and electronic properties

UV–vis diffuse reflectance spectra (DRS) and Mott-Schottky (M-S) measurements were carried out in order to investigate the light absorption ability and electronic band structure of the photocatalysts. As shown in Fig. 4a, TpBD COF exhibits strong light-harvesting ability in the visible region, with an absorption edge at 770 nm, arising from the π-π * electron transition of the large conjugation systems. In contrast, ZIS displays an absorption edge at 570 nm, corresponding to the intrinsic band gap of ZIS [25]. After coupling with TpBD COF, the absorption of ZIS in the visible region is largely broadened, which is beneficial to the photocatalytic performance. The band gap (E_g) of TpBD COF (2.12 eV) and ZIS (2.35 eV) can be obtained by Tauc-plots based on the UV–vis absorption spectra (Fig. 4b-c), respectively [53]. The M-S plots of TpBD COF and ZIS samples show positive slopes (Fig. 4d-e), demonstrating their n-type semiconductor features. It is generally accepted that the CB potential of n-type semiconductors is close to the flat band potential [54,55]. Therefore, the CB potentials of TpBD COF and ZIS are determined to be − 1.12 V and − 1.56 V vs Ag/AgCl@pH7, or − 0.51 V and − 0.95 V vs NHE@pH0, respectively (Eq. 1).
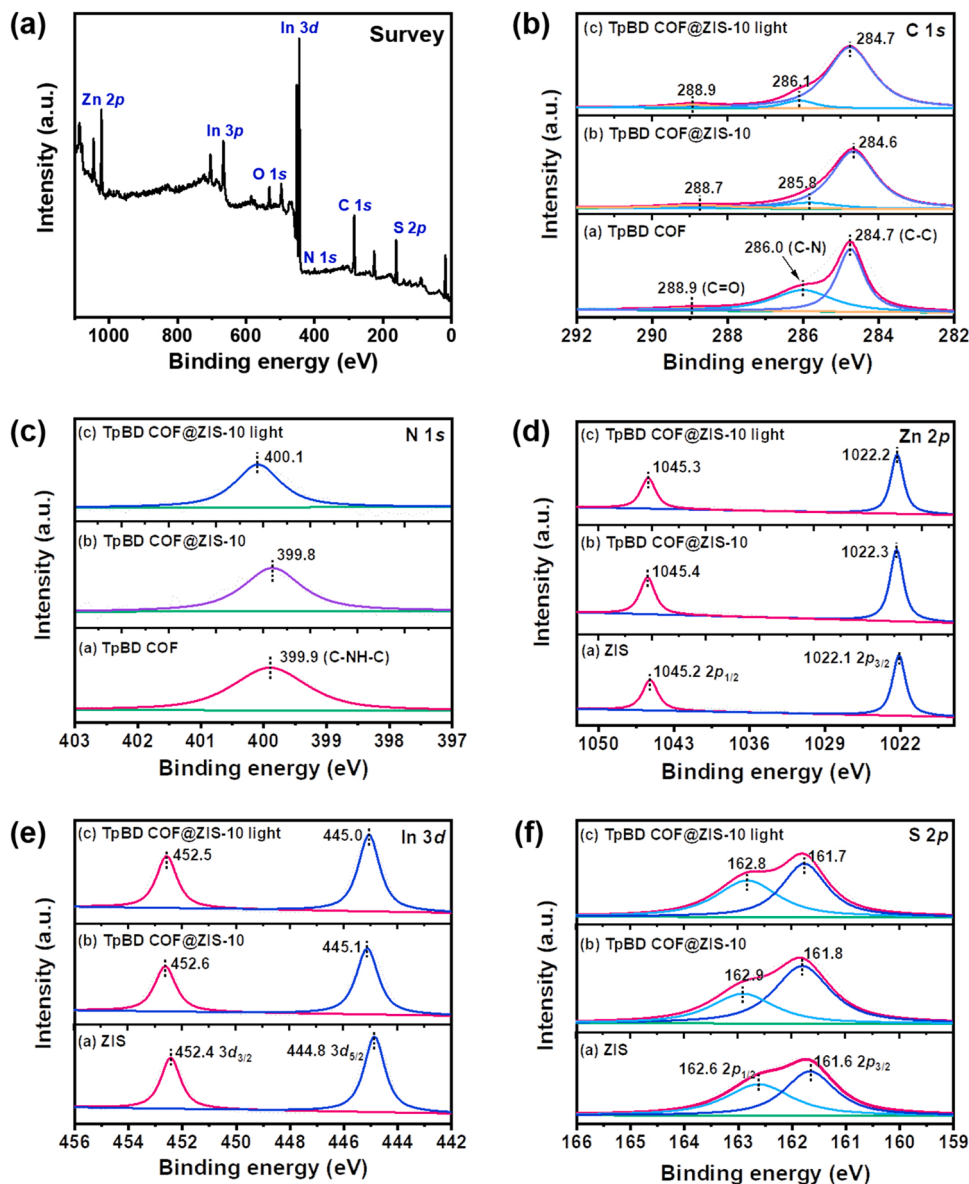
Fig. 3. XPS survey spectrum of TpBD COF@ZIS-10 sample (a), along with high-resolution XPS spectra of C 1 s (b), N 1 s (c), Zn 2p (d), In 3d (e) and S 2p (f) regions.

$$E_{\text{NHE}} = E_{\text{RHE}} - 0.0591\ \text{pH} \tag{1}$$

As the bandgap of TpBD COF and ZIS are 2.12 eV and 2.35 eV (Figs. 4b and 4c), the VB potentials of TpBD COF and ZIS are determined to be 1.61 V and 1.40 V vs NHE@pH0, respectively. The obtained electronic band structures of TpBD COF and ZIS are compared in Fig. 4f.

Based on the negative CB positions of TpBD COF and ZIS, and comparing their redox potential with that of H$^+$/H$_2$ (0 V vs NHE@pH0), it can be predicted that both TpBD COF and ZIS are appropriate visible-light-response photocatalysts with strong reduction ability of CB electrons.

The VB potentials of TpBD COF and ZIS were further determined by VB XPS ($E_{\text{VB, XPS}}$), and the obtained values are approximately 1.33 eV and 1.12 eV, respectively (Fig. S6). Based on the conversion formula (Eq. 2) [46],

$$E_{\text{VB, NHE}} = \varphi + E_{\text{VB, XPS}} - 4.44 \tag{2}$$

where φ is the electron work function of the analyzer (4.20 eV), the calculated VB positions of TpBD COF and ZIS are 1.51 V and 1.30 V vs

NHE@pH0, respectively, which are very close to the values obtained from the photoelectrochemical measurements (Fig. 4f).

3.5. DFT computational calculations

The band structures of TpBD COF and ZIS were analyzed by DFT calculations. Figs. 5a and 5b show that the calculated E_g values of TpBD COF (1.89 eV) and ZIS (2.09 eV) are very close to the experimental results (Fig. 4b-c). The electrostatic potentials of the photocatalysts were calculated to quantify the band offset of the TpBD COF@ZIS heterojunction. As shown in Fig. 5c, the CB offset ($\triangle E_{\text{CBO}}$) and the VB offset ($\triangle E_{\text{VBO}}$) of TpBD COF and ZIS are 0.41 eV and 0.21 eV, respectively. These results clearly demonstrate the staggered band alignment structure of TpBD COF@ZIS heterojunction [56,57].

Moreover, DFT calculations can provide an efficient way to study the interface interaction and charge transfer pathway at the interfaces of the heterojunction [58]. The work function (Φ) is a vital parameter to determine the interface charge transfer. It can be calculated using Eq. (3):

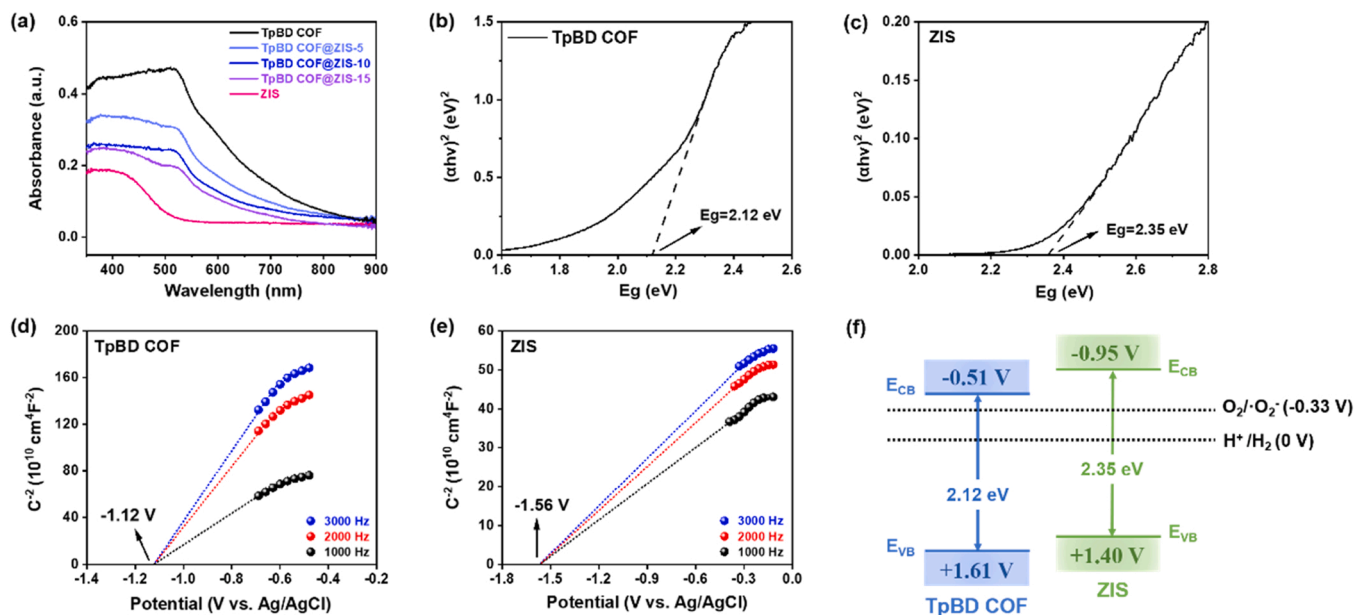$$\Phi = E_{\text{vac}} - E_{\text{F}} \tag{3}$$

Fig. 4. UV–vis absorption spectra of the photocatalysts (a) and corresponding $(\alpha h\nu)^2$ versus $h\nu$ plots for TpBD COF (b) and ZIS (c). Mott-Schottky plots for TpBD COF (d) and ZIS (e). Determined electronic band structures of TpBD COF and ZIS (f).
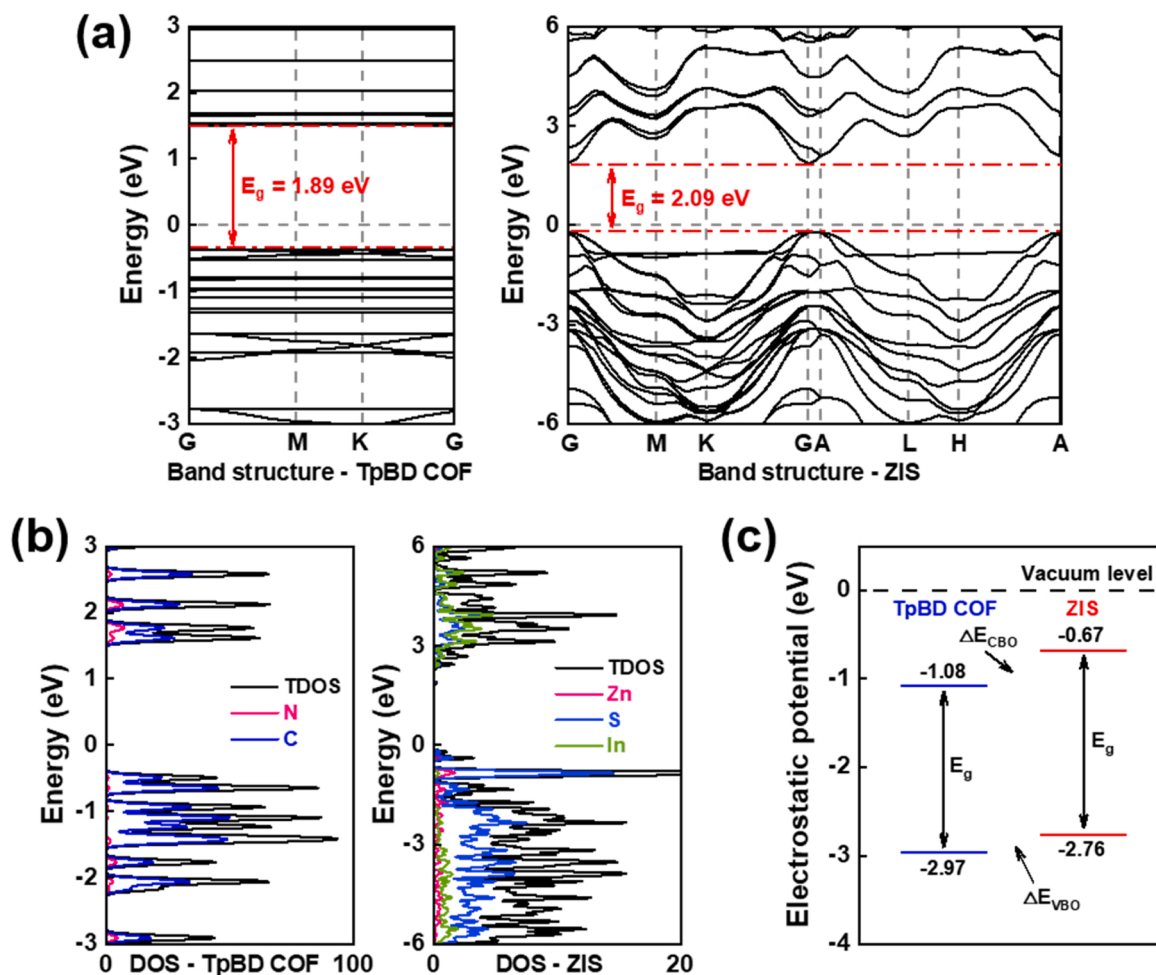

Fig. 5. (a) Band structures and (b) density of states of TpBD COF and ZIS. (c) Energy band offset of the TpBD COF@ZIS heterojunction.

where E_{vac} is the potential of vacuum energy, while E_F is the Fermi energy.

As indicated in Fig. 6a-b, the Φ of TpBD COF (001) surface and ZIS (102) surface are 6.12 and 5.81 eV, respectively. The difference in work function can cause charge transfer at the interface of TpBD COF and ZIS. As TpBD COF has larger Φ, electrons will transfer from ZIS to TpBD COF until the E_F equilibrium is reached. This results in a positively charged interface for ZIS with upward interface band bending. In contrast, TpBD COF is negatively charged and exhibits downward interface band bending at the interface, resulting in electron accumulation. This creates an IEF that promotes electron transfer from ZIS to TpBD COF, as confirmed by the XPS characterization results. In order to unveil the interfacial electronic interaction, the average charge density difference of TpBD COF@ZIS heterojunction were calculated (Fig. 6c). $\triangle n_e$ reflects the difference in plane averaged charge density along the Z axis. A positive value of $\triangle n_e$ indicates accumulation of electrons. The results show strong coupling effects at the interface of TpBD COF and ZIS, with electron migration direction in agreement with Φ and XPS analyses. These calculations further confirm the electron migration direction of a S-scheme heterojunction.

3.6. Photocatalytic activity evaluation

Hydrogen production was used to evaluate the photoreactivity of the photocatalysts. Several sacrificial agents, including Na_2S/Na_2SO_3, TEOA, L-Ascorbic acid and Lactic acid, were used to evaluate their effect on the photocatalytic water splitting performance to produce H_2 (Fig. S7a). The highest H_2 production rate (2304 $\mu mol\ g^{-1}\ h^{-1}$) was achieved when L-Ascorbic acid was used as sacrificial agent. It is reported that an acidic medium can cause a smaller water dissociation barrier, which is beneficial to H_2 production [59]. Furthermore, L-Ascorbic acid has a lower oxidation potential and is easily oxidized by holes [60,61], being an ideal sacrificial agent for this work. The mass of the composite photocatalysts powder was optimized, with 25 mg being the optimal value for the highest H_2 production (Fig. S7b). Therefore, the optimal conditions were 25 mg photocatalyst (without co-catalyst) dispersed in 50 mL aqueous solution, with 0.05 M L-Ascorbic acid as sacrificial agent, under visible-light irradiation ($\lambda > 420$ nm) using a 300 W Xenon arc lamp. Control experiments were conducted to exclude the possibilities of the sacrificial agent to produce H_2 under visible-light and the photocatalyst to react with the sacrificial agent to produce H_2 in the dark (Fig. S8).

Fig. 7a summarizes the photocatalytic water splitting performance to produce H_2 of TpBD COF@ZIS-X composites, under the same conditions. After 3 h of visible-light irradiation, a comparatively small amount of H_2 (423 $\mu mol\ g^{-1}$) was detected for pure TpBD COF, while an apparent amount of H_2 (702 $\mu mol\ g^{-1}$) was observed for pure ZIS. Fig. 7b shows the values of the photocatalytic H_2 production for the different materials. The optimal H_2 production rate of TpBD COF@ZIS-10 reaches 2304 $\mu mol\ g^{-1}\ h^{-1}$, which is around 16.3 and 9.8 times higher than the values of TpBD COF and ZIS, respectively. It is worth noting that the photocatalytic H_2 production rate of TpBD COF@ZIS-10, obtained by
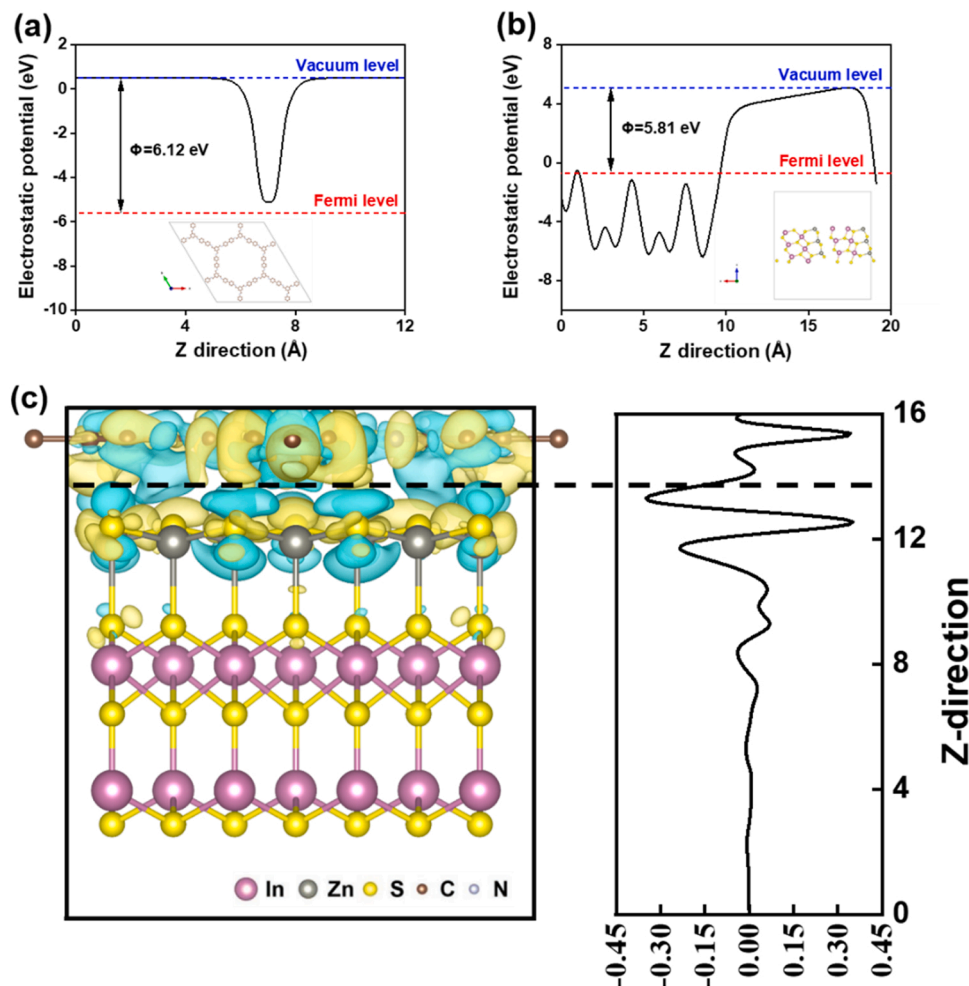

Fig. 6. Electrostatic potential of (a) TpBD COF and (b) ZIS (insets show the models of TpBD COF and ZIS used for the calculations). (c) Planar averaged charge density difference for the TpBD COF@ZIS heterojunction model (blue regions indicate electrons consumption and yellow regions indicate electrons accumulation).
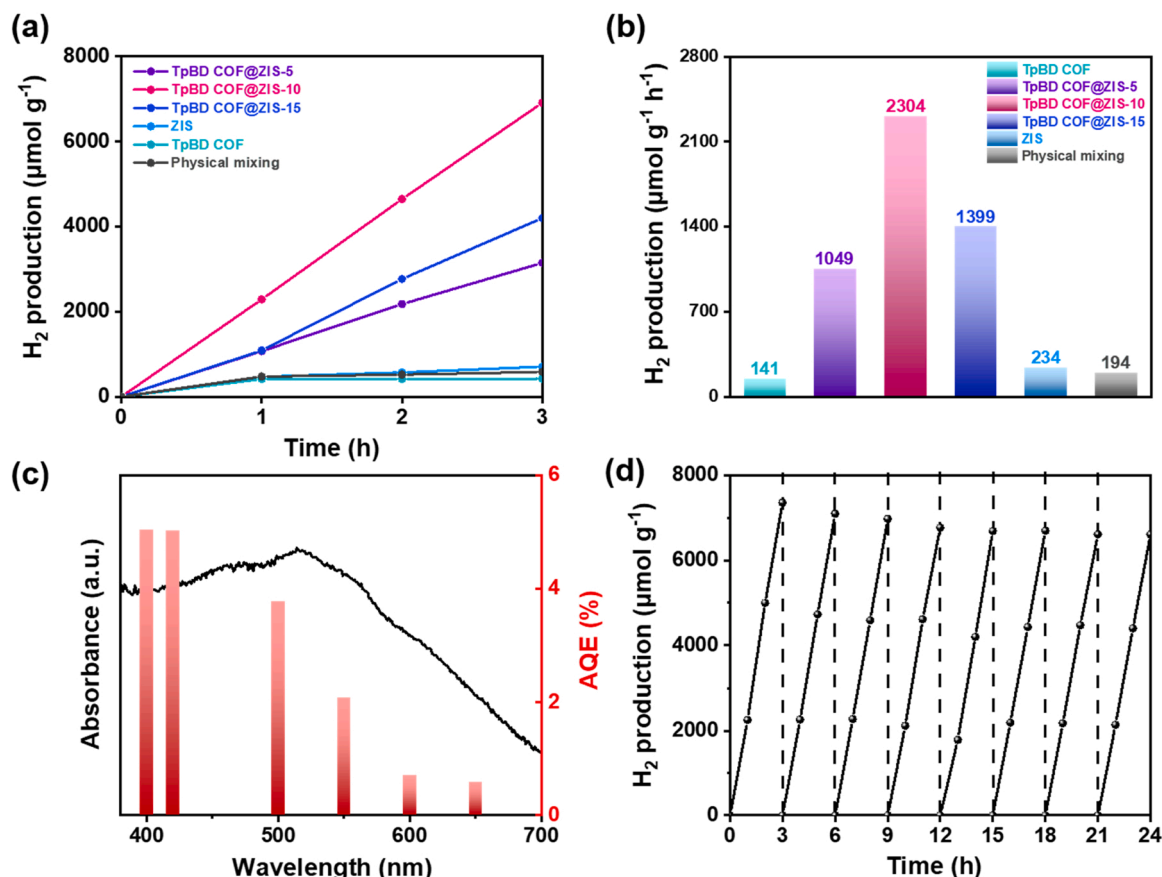
Fig. 7. (a) Time-dependent H_2 evolution curves. (b) Effect of ZIS loading amount on the H_2 production rate of TpBD COF@ZIS. (c) AQE for TpBD COF@ZIS-10 at different wavelengths. (d) Recycling tests for TpBD COF@ZIS-10, showing the stability of H_2 production rate over eight reaction cycles of 3 h each.

the microwave-hydrothermal method, is around 11.8 times higher than the rate measured for the physically mixed sample (with a ZIS:TpBD COF mass ratio of 10:1), indicating that a well integrated heterojunction is essential for an efficient photocatalytic H_2 production.

Fig. 7c displays the AQE of TpBD COF@ZIS-10 under different wavelengths of monochromatic light irradiation. The trend is consistent with the UV–vis absorption strength, showing an AQE value of 5.02% at 420 nm. Such performance is comparable (and, in some cases, higher) than most reported results for ZIS-based photocatalysts (Table S1) and other COF-based heterojunction photocatalysts (Table S2). In addition, when Pt is loaded on the TpBD COF@ZIS-10 composite, as co-catalyst, in form of nanoparticles (NPs), the photocatalytic water splitting, leading to H_2 production, is significantly enhanced (Figs. S9a-b). When the mass ratio of Pt NPs is 0.4 wt%, the H_2 production rate reaches the highest value (7551 μmol g^{-1} h^{-1}).

In addition, the stability of the photocatalyst is also a vital performance indicator. As displayed in Fig. 7d, TpBD COF@ZIS-10 is still able to maintain a high H_2 production rate of 2202 μmol g^{-1} h^{-1}, even after 8 reaction cycles (of 3 h per cycle). Moreover, the XRD patterns and FTIR spectra of the used TpBD COF@ZIS-10 sample (Figs. S10a-b) show no significant changes, except for a slight weakening of the peak intensity, demonstrating that the structure of the composite remains intact after the reaction. This is further supported by the SEM image of the used TpBD COF@ZIS-10 (Fig. S11), which confirms that the morphology of the material is maintained after the reaction.

3.7. Photoelectrochemical property analysis

In order to unveil the photocatalytic mechanism of the TpBD COF@ZIS heterojunction, the photoelectric properties of the

photocatalysts were compared. Electrochemical impedance spectroscopy (EIS) was used to monitor the electron mobility of the photogenerated carriers. Fig. 8a displays the EIS spectra of TpBD COF, ZIS and TpBD COF@ZIS-10 samples. The TpBD COF@ZIS-10 sample shows the smallest semicircle, suggesting the lowest charge-transfer resistance. The Rct values, obtained by fitting the simulated electrical equivalent circuit model (inset of Fig. 8a), decrease in the order of TpBD COF (9183 Ω) > ZIS (8413 Ω) > TpBD COF@ZIS-10 (7097 Ω), as shown in Table S3. This suggests that the TpBD COF@ZIS-10 heterojunction has the highest efficiency in electron transfer due to its lowest interfacial resistance [62,63]. These results provide valuable insights into the photoelectrochemical properties of the TpBD COF@ZIS heterojunction and demonstrate its potential as an efficient photocatalyst for hydrogen production.

Steady-state photoluminescence (PL) spectra provide another way to investigate the behavior of photogenerated charge carriers, as the emission of fluorescence arises from charge recombination. Therefore, the intensity of the PL spectra can be used to qualitatively monitor the separation or recombination efficiencies of the photocatalysts. As shown in Fig. 8b, the PL emission intensity of TpBD COF@ZIS-10 is noticeably weaker than the values of pure TpBD COF and ZIS, demonstrating that the heterojunction construction can retard the recombination of photogenerated electron-hole pairs by providing an efficient pathway for charge migration [64,65]. The transient photocurrent response (TPR) and the surface photovoltage spectroscopy (SPS) response allow to further investigate the charge separation efficiency. The TPR of TpBD COF@ZIS-10 is obviously higher than those of TpBD COF and ZIS, suggesting that the heterojunction allows more efficient charge separation (Fig. 8c). Moreover, the SPS response intensity of TpBD COF@ZIS-10 is also stronger than the other materials (Fig. S12).
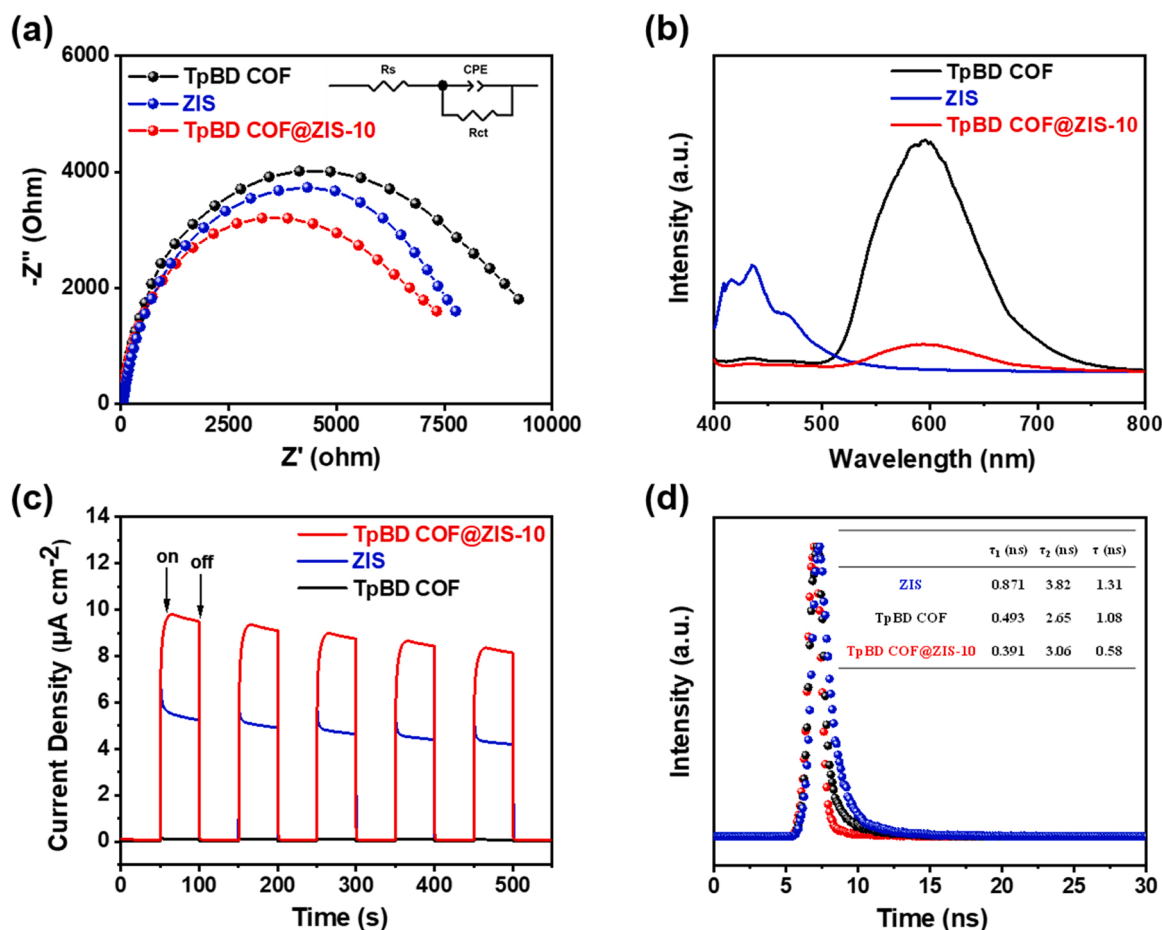
Fig. 8. (a) Nyquist plots of EIS, (b) steady-state PL spectra (λ_{Ex} =380 nm), (c) TPR spectra and (d) TRPL results of TpBD COF, ZIS and TpBD COF@ZIS-10.

All the above results indicate that the TpBD COF@ZIS heterojunction can effectively stimulate the separation of photogenerated electron-hole pairs. To further understand the charge transfer process, time-resolved photoluminescence (TRPL) spectra characterization was also carried out. From Fig. 8d, it is evident that the average emission lifetime of TpBD COF@ZIS (sample TpBD COF@ZIS-10) is shorter than the values of TpBD COF and ZIS, respectively. The significantly reduced lifetime confirms that an electron transfer pathway between TpBD COF and ZIS is formed in a nonradiative quenching manner [66].

Based on the above analyses, we can summarize the key factors of the TpBD COF@ZIS heterojunction, which include improved light-harvesting ability and stimulated charge separation. These factors are decisive to improve the photocatalytic activity for H_2 production [67, 68].

3.8. Photocatalytic H_2 mechanism

In order to better understand the charge transfer pathway in the TpBD COF@ZIS heterojunction, electron spin resonance (ESR) analyses were conducted. Before measurements, the mixture of methanol/DMPO/photocatalyst was illuminated for 300 s. As the CB potentials of TpBD COF (-0.51 V vs. NHE@pH0) and ZIS (-0.95 V vs. NHE@pH0) thermodynamically favor the reduction of O_2 by CB electrons to produce $\bullet O_2^-$ radicals ($E_{O2/\bullet O2-} = -0.33$ V), it is not surprising to detect signals of $\bullet O_2^-$ radicals in suspensions of TpBD COF and ZIS (Fig. S13) [69,70]. As the CB potential of ZIS is more negative compared to that of TpBD COF, ZIS exhibits stronger $\bullet O_2^-$ signal intensity. However, a sharply increased $\bullet O_2^-$ signal is observed for TpBD COF@ZIS-10, indicating that the coupling of TpBD COF with ZIS can provide more active sites for redox

reaction due to efficient charge carrier separation.

If a type-II heterojunction is formed between TpBD COF and ZIS (as illustrated in Fig. S14), the photogenerated electrons in the CB of ZIS will migrate to the CB of TpBD COF. Simultaneously, holes in the VB of TpBD COF will transfer to the VB of ZIS. To clarify the charge transfer pathway and redox ability of the TpBD COF@ZIS heterojunction, it is important to consider the relative positions of the CB and VB potentials of TpBD COF and ZIS. In particular, the CB potential of TpBD COF will determine its reduction capability, while the VB potential of ZIS will determine its oxidation ability. However, it is inconsistent with the radical trapping experimental results to suggest that the reduction of O_2 to produce $\bullet O_2^-$ radicals will become difficult due to the reduced redox ability of the heterojunction. This suggests that a different charge transfer mechanism is taking place. In contrast, the S-scheme charge transfer pathway provides a more reasonable explanation for the experimental findings.

Based on the electronic band structures (Fig. 9a), ZIS can act as a reduction-type photocatalyst with higher Fermi level (work function of 5.81 eV), while TpBD COF can perform as an oxidation-type photocatalyst with lower Fermi level (work function of 6.12 eV). When TpBD COF closely contacts ZIS, the electrons in ZIS will spontaneously transfer to TpBD COF at the interface until the equilibrium of the Fermi levels is reached (Fig. 9b). Thus, the surface of ZIS will be positively charged due to the loss of electrons, while the surface of TpBD COF will be negatively charged due to the acceptance of electrons. Therefore, an IEF will be simultaneously produced at the heterojunction interface, together with upward bending edge of ZIS and downward bending energy of TpBD COF. Then, the combined influence of IEF, band edge bending and Coulombic attraction will result in the production of a S-scheme charge
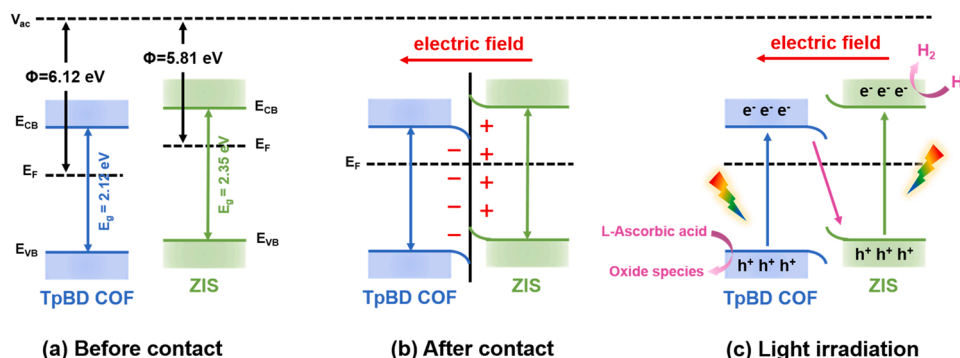
Fig. 9. S-scheme charge transfer process.

transfer pathway. Under visible-light irradiation, the photogenerated electrons on the CB of TpBD COF will simultaneously migrate to the VB of ZIS to combine with the holes, resulting in the accumulation of CB electrons at the interface of ZIS for H_2 production. At the same time, the accumulated holes at the VB of TpBD COF can facilitate the oxidation of L-Ascorbic acid (Fig. 9c). Eventually, the reduction and oxidation ability of TpBD COF@ZIS heterojunction will be decided by the electrons at the CB of ZIS and holes on the VB of TpBD COF, respectively. Then, the maximized redox ability of S-scheme TpBD COF@ZIS heterojunction provides a strong driving force for photocatalytic H_2 production. Therefore, it is not strange to see an accelerated production of $\bullet O_2^-$ radicals after coupling TpBD COF with ZIS (Fig. S13).

To provide further evidence supporting the S-scheme heterojunction mechanism, in-situ XPS measurements were performed. The results shown in Fig. 3b-c indicate that under 420 nm light illumination, the binding energies of C 1 *s* and N 1 *s* in TpBD COF@ZIS-10 sample upshift, compared with the results obtained in the dark. In contrast, the binding energies of Zn 2*p*, In 3*d* and S 2*p* in TpBD COF@ZIS-10 sample negatively shift, compared to those detected in the dark (Fig. 3d-f). These results confirm that the photogenerated electrons are able to migrate from TpBD COF to ZIS, upon illumination. Based on all the above results, it is reasonable to propose a S-scheme charge transfer mechanism to explain the TpBD COF@ZIS heterojunction in water splitting to produce H_2 under visible-light irradiation.

4. Conclusions

Novel hybridized photocatalysts, TpBD COF@ZIS, were successfully obtained by in-situ growth of ZIS on the surface of TpBD COF. The optimal photocatalyst (TpBD COF@ZIS-10) showed a significantly enhanced H_2 production rate of 2304 μmol g^{-1} h^{-1} with an AQE of 5.02%, at 420 nm, under visible-light irradiation, even in the absence of a co-catalyst. In addition, TpBD COF@ZIS-10 exhibited excellent recycling stability after 8 reaction cycles. Through in-situ XPS, ESR and DFT calculations, a S-scheme charge transfer mechanism was proposed to explain the enhanced photocatalytic performance of TpBD COF@ZIS-10. Strong interaction at the interface and the S-scheme charge transfer mechanism between TpBD COF and ZIS promoted charge separation/migration and retarded recombination. The findings of this work provide new valuable insights for the design and synthesis of innovative S-scheme heterojunction photocatalysts.

CRediT authorship contribution statement

Shutong Bao: Data curation, Formal analysis, Writing – original draft. **Qiuyan Tan:** Investigation, Formal analysis. **Shaodan Wang:** Investigation, Formal analysis. **Jie Guo:** Investigation, Formal analysis. **Kangle Lv:** Conceptualization, Formal analysis, Resources, Writing – review & editing. **Sónia A.C. Carabineiro:** Resources, Writing – review & editing. **Lili Wen:** Conceptualization, Project administration,

Resources, Writing – review & editing.

Declaration of Competing Interest

The authors declare that they have no known competing financial interests or personal relationships that could have appeared to influence the work reported in this paper.

Data Availability

Data will be made available on request.

Appendix A. Supporting information

Supplementary data associated with this article can be found in the online version at doi:10.1016/j.apcatb.2023.122624.

References

[1] N.S. Lewis, Toward cost-effective solar energy use, Science 315 (2007) 798–801.
[2] N. Armaroli, V. Balzani, The future of energy supply: challenges and opportunities, Angew. Chem. Int. Ed. 46 (2007) 52–66.
[3] K.N. Li, S.S. Zhang, Y.H. Li, J.J. Fan, K.L. Lv, MXenes as noble-metal-alternative co-catalysts in photocatalysis, Chin. J. Catal. 42 (2021) 3–14.
[4] L. Chen, X.L. Song, J.T. Ren, Z.Y. Yuan, Precisely modifying Co$_2$P/black TiO$_2$ S-scheme heterojunction by in situ formed P and C dopants for enhanced photocatalytic H$_2$ production, Appl. Catal. B: Environ. 315 (2022), 121546.
[5] X.C. Wang, K. Maeda, X.F. Chen, K. Takanabe, K. Domen, Y.D. Hou, X.Z. Fu, M. Antonietti, Polymer semiconductors for artificial photosynthesis: hydrogen evolution by mesoporous graphitic carbon nitride with visible light, J. Am. Chem. Soc. 131 (2009) 1680–1681.
[6] W. Zhou, W. Li, J.Q. Wang, Y. Qu, Y. Yang, Y. Xie, K.F. Zhang, L. Wang, H.G. Fu, D. Y. Zhao, Ordered mesoporous black TiO$_2$ as highly efficient hydrogen evolution photocatalyst, J. Am. Chem. Soc. 136 (2014) 9280–9283.
[7] Y. Pan, X.Z. Yuan, L.B. Jiang, H.B. Yu, J. Zhang, H. Wang, R.P. Guan, G.M. Zeng, Recent advances in synthesis, modification and photocatalytic applications of micro/nano-structured zinc indium sulfide, Chem. Eng. J. 354 (2018) 407–431.

[8] J. Fan, J. Lei, L.M. Wang, C.Z. Yu, B. Tu, D.Y. Zhao, Rapid and high-capacity immobilization of enzymes based on mesoporous silicas with controlled morphologies, Chem. Commun. (2003) 2140–2141.

[9] X.C. Jiao, Z.W. Chen, X.D. Li, Y.F. Sun, S. Gao, W.S. Yan, C.M. Wang, Q. Zhang, Y. Lin, Y. Luo, Y. Xie, Defect-mediated electron-hole separation in one-unit-cell ZnIn₂S₄ layers for boosted solar-driven CO₂ reduction, J. Am. Chem. Soc. 139 (2017) 7586–7594.

[10] W.L. Yang, L. Zhang, J.F. Xie, X.D. Zhang, Q.H. Liu, T. Yao, S.Q. Wei, Q. Zhang, Y. Xie, Enhanced photoexcited carrier separation in oxygen-doped ZnIn₂S₄ nanosheets for hydrogen evolution, Angew. Chem. Int. Ed. 55 (2016) 6716–6720.

[11] X.D. Jing, N. Lu, J.D. Huang, P. Zhang, Z.Y. Zhang, One-step hydrothermal synthesis of S-defect-controlled ZnIn₂S₄ microflowers with improved kinetics process of charge-carriers for photocatalytic H₂ evolution, J. Energy Chem. 58 (2021) 397–407.

[12] J.W. Fu, J.G. Yu, C.J. Jiang, B. Cheng, g-C₃N₄-based heterostructured photocatalysts, Adv. Energy Mater. 8 (2018), 1701503.

[13] R. Boppella, C.H. Choi, J. Moon, D.H. Kim, Spatial charge separation on strongly coupled 2D-hybrid of rGO/La₂Ti₂O₇/NiFe-LDH heterostructures for highly efficient noble metal free photocatalytic hydrogen generation, Appl. Catal. B: Environ. 239 (2018) 178–186.

[14] S.A. Rawool, M.R. Pai, A.M. Banerjee, A. Arya, R.S. Ningthoujam, R. Tewari, R. Rao, B. Chalke, P. Ayyub, A.K. Tripathi, S.R. Bharadwaj, pn Heterojunctions in NiO: TiO₂ composites with type-II band alignment assisting sunlight driven photocatalytic H₂ generation, Appl. Catal. B: Environ. 221 (2018) 443–458.

[15] S.J. Li, M.J. Cai, Y.P. Liu, C.C. Wang, K.L. Lv, X.B. Chen, S-Scheme photocatalyst TaON/Bi₂WO₆ nanofibers with oxygen vacancies for efficient abatement of antibiotics and Cr(VI): Intermediate eco-toxicity analysis and mechanistic insights, Chin. J. Catal. 43 (2022) 2652–2664.

[16] K.N. Li, W.C. Zhou, X.F. Li, Q. Li, S.A.C. Carabineiro, S.S. Zhang, J.J. Fan, K.L. Lv, Synergistic effect of cyano defects and CaCO₃ in graphitic carbon nitride nanosheets for efficient visible-light-driven photocatalytic NO removal, J. Hazard. Mater. 442 (2023) 130040.

[17] S.K. Lakhera, H.Y. Hafeez, P. Veluswamy, V. Ganesh, A. Khan, H. Ikeda, B. Neppolian, Enhanced photocatalytic degradation and hydrogen production activity of in situ grown TiO₂ coupled NiTiO₃ nanocomposites, Appl. Surf. Sci. 449 (2018) 790–798.

[18] W.L. Yu, S. Zhang, J.X. Chen, P.F. Xia, M.H. Richter, L.F. Chen, W. Xu, J.P. Jin, S. L. Chen, T.Y. Peng, Biomimetic Z-scheme photocatalyst with a tandem solid-state electron flow catalyzing H₂ evolution, J. Mater. Chem. A 6 (2018) 15668–15674.

[19] W.L. Yu, J.X. Chen, T.T. Shang, L.F. Chen, L. Gu, T.Y. Peng, Direct Z-scheme g-C₃N₄/WO₃ photocatalyst with atomically defined junction for H₂ production, Appl. Catal. B: Environ. 219 (2017) 693–704.

[20] Q.P. Lu, Y.F. Yu, Q.L. Ma, B. Chen, H. Zhang, 2D transition-metal-dichalcogenide-nanosheet-based composites for photocatalytic and electrocatalytic hydrogen evolution reactions, Adv. Mater. 28 (2016) 1917–1933.

[21] Y.G. Chao, P. Zhou, J.P. Lai, W.Y. Zhang, H.W. Yang, S.Y. Lu, H. Chen, K. Yin, M. G. Li, L. Tao, C.S. Shang, M.P. Tong, S.J. Guo, Ni₁₋ₓCoₓSe₂-C/ZnIn₂S₄ hybrid nanocages with strong 2D/2D hetero-interface interaction enable efficient h₂-releasing photocatalysis, Adv. Funct. Mater. 31 (2021), 2100923.

[22] F.H. Mu, Q. Cai, H. Hu, J. Wang, Y. Wang, S.J. Zhou, Y. Kong, Construction of 3D hierarchical microarchitectures of Z-scheme UiO-66-(COOH)₂/ZnIn₂S₄ hybrid decorated with non-noble MoS₂ cocatalyst: a highly efficient photocatalyst for hydrogen evolution and Cr(VI) reduction, Chem. Eng. J. 384 (2020) 123352.

[23] P.X. Jin, L. Wang, X.L. Ma, R. Lian, J.W. Huang, H.D. She, M.Y. Zhang, Q.Z. Wang, Construction of hierarchical ZnIn₂S₄@PCN-224 heterojunction for boosting photocatalytic performance in hydrogen production and degradation of tetracycline hydrochloride, Appl. Catal. B: Environ. 284 (2021) 119762.

[24] Y.X. Li, K. Zhang, S.Q. Peng, G.X. Lu, S.B. Li, Photocatalytic hydrogen generation in the presence of ethanolamines over Pt/ZnIn₂S₄ under visible light irradiation, J. Mol. Catal. A: Chem. 363–364 (2012) 354–361.

[25] H. Liu, J. Zhang, D. Ao, Construction of heterostructured ZnIn₂S₄@NH₂-MIL-125 (Ti) nanocomposites for visible-light-driven H₂ production, Appl. Catal. B: Environ. 221 (2018) 433–442.

[26] Y.Y. Qin, H. Li, J. Lu, Y.H. Feng, F.Y. Meng, C.C. Ma, Y.S. Yan, M.J. Meng, Synergy between van der waals heterojunction and vacancy in ZnIn₂S₄/g-C₃N₄ 2D/2D photocatalysts for enhanced photocatalytic hydrogen evolution, Appl. Catal. B: Environ. 277 (2020), 119254.

[27] X.Y. Cai, Z.T. Zeng, Y.D. Liu, Z.H. Li, X.Q. Gu, Y.L. Zhao, L. Mao, J.Y. Zhang, Visible-light-driven water splitting by yolk-shelled ZnIn₂S₄-based heterostructure without noble-metal co-catalyst and sacrificial agent, Appl. Catal. B: Environ. 297 (2021) 120391.

[28] G.C. Zuo, Y.T. Wang, W.L. Teo, Q.M. Xian, Y.L. Zhao, Direct Z-scheme TiO₂-ZnIn₂S₄ nanoflowers for cocatalyst-free photocatalytic water splitting, Appl. Catal. B: Environ. 291 (2021) 120126.

[29] M.Y. Zhao, S. Liu, D.M. Chen, S.S. Zhang, S.A.C. Carabineiro, K.L. Lv, A novel S-scheme 3D ZnIn₂S₄/WO₃ heterostructure for improved hydrogen production under visible light irradiation, Chin. J. Catal. 43 (2022) 2615–2624.

[30] J.W. Fu, Q.L. Xu, J.X. Low, C.J. Jiang, J.G. Yu, Ultrathin 2D/2D WO₃/g-C₃N₄ step-scheme H₂-production photocatalyst, Appl. Catal. B: Environ. 243 (2019) 556–565.

[31] Y.P. Zhang, W. Han, Y. Yang, H.Y. Zhang, Y. Wang, L. Wang, X.J. Sun, F.M. Zhang, S-scheme heterojunction of black TiO₂ and covalent-organic framework for enhanced photocatalytic hydrogen evolution, Chem. Eng. J. 446 (2022) 137213.

[32] H. Wang, H. Wang, Z.W. Wang, L. Tang, G.M. Zeng, P. Xu, M. Chen, T. Xiong, C. Y. Zhou, X.Y. Li, D.L. Huang, Y. Zhu, Z.X. Wang, J.W. Tang, Covalent organic framework photocatalysts: structures and applications, Chem. Soc. Rev. 49 (2020) 4135–4165.

[33] X.Y. Chen, K.Y. Geng, R.Y. Liu, K. Tian, Y.F. Gong, Z.P. Li, S.S. Tao, Q.H. Jiang, D. L. Jiang, Covalent organic frameworks: chemical approaches to designer structures and built-in functions, Angew. Chem. Int. Ed. 59 (2020) 5050–5091.

[34] J.J. Wang, L.Z. Wang, Y. Wang, F. Yang, J.W. Li, X.Y. Guan, J.J. Zong, F. Zhou, J. H. Huang, Y.N. Liu, Covalently connected core-shell NH₂-UiO-66@Br-COFs hybrid materials for CO₂ capture and I₂ vapor adsorption, Chem. Eng. J. 438 (2022), 135555.

[35] Y.Y. Wan, L. Wang, H.X. Xu, X.J. Wu, J.L. Yang, A simple molecular design strategy for two-dimensional covalent organic framework capable of visible-light-driven water splitting, J. Am. Chem. Soc. 142 (2020) 4508–4516.

[36] W.B. Chen, L. Wang, D.Z. Mo, F. He, Z.L. Wen, X.J. Wu, H.X. Xu, L. Chen, Modulating benzothiadiazole-based covalent organic frameworks via halogenation for enhanced photocatalytic water splitting, Angew. Chem. Int. Ed. 132 (2020) 17050–17057.

[37] P.F. Wei, M.Z. Qi, Z.P. Wang, S.Y. Ding, W. Yu, Q. Liu, L.K. Wang, H.Z. Wang, W. K. An, W. Wang, Benzoxazole-linked ultrastable covalent organic frameworks for photocatalysis, J. Am. Chem. Soc. 140 (2018) 4623–4631.

[38] S.Z. Yang, W.H. Hu, X. Zhang, P.L. He, B. Pattengale, C.M. Liu, M. Cendejas, I. Hermans, X.Y. Zhang, J. Zhang, J. Huang, 2D covalent organic frameworks as intrinsic photocatalysts for visible light-driven CO₂ reduction, J. Am. Chem. Soc. 140 (2018) 14614–14618.

[39] S. Wang, Q. Sun, W. Chen, Y.Q. Tang, B. Aguila, Y.X. Pan, A.M. Zheng, Z.Y. Yang, L. Wojtas, S.Q. Ma, F.S. Xiao, Programming covalent organic frameworks for photocatalysis: investigation of chemical and structural variations, Matter 2 (2020) 416–427.

[40] S. Chandra, S. Kandambeth, B.P. Biswal, B. Lukose, S.M. Kunjir, M. Chaudhary, R. Babarao, T. Heine, R. Banerjee, Chemically stable multilayered covalent organic nanosheets from covalent organic frameworks via mechanical delamination, J. Am. Chem. Soc. 135 (2013) 17853–17861.

[41] B.P. Biswal, S. Chandra, S. Kandambeth, B. Lukose, T. Heine, R. Banerjee, Mechanochemical synthesis of chemically stable isoreticular covalent organic frameworks, J. Am. Chem. Soc. 135 (2013) 5328–5331.

[42] J.H. Chong, M. Sauer, B.O. Patrick, M.J. MacLachlan, Highly stable keto-enamine salicylideneanilines, Org. Lett. 5 (2003) 21.

[43] N. Nie, L.Y. Zhang, J.W. Fu, B. Cheng, J.G. Yu, Self-assembled hierarchical direct Z-scheme g-C₃N₄/ZnO microspheres with enhanced photocatalytic CO₂ reduction performance, Appl. Surf. Sci. 441 (2018) 12–22.

[44] C.X. Zhao, H.L. Jiang, Q. Liang, M. Zhou, Y.Z. Zhang, Z.Y. Li, S. Xu, NH₂-UiO-66 with heterogeneous pores assists zinc indium sulfide in accelerating the photocatalytic H₂ evolution under visible-light irradiation, Sol. Energy 207 (2020) 599–608.

[45] B.B. Liu, X.J. Liu, J.Y. Liu, C.J. Feng, Z. Li, C. Li, Y.Y. Gong, L.K. Pan, S.Q. Xu, C. Q. Sun, Efficient charge separation between UiO-66 and ZnIn₂S₄ flowerlike 3D microspheres for photoelectronchemical properties, Appl. Catal. B: Environ. 226 (2018) 234–241.

[46] M.X. Tan, Y. Ma, C.Y. Yu, Q.J. Luan, J.J. Li, C.B. Liu, W.J. Dong, Y.J. Su, L.J. Qiao, L. Gao, Q.P. Lu, Y. Bai, Boosting photocatalytic hydrogen production via interfacial engineering on 2D ultrathin Z-scheme ZnIn₂S₄/g-C₃N₄ heterojunction, Adv. Funct. Mater. 32 (2022), 2111740.

[47] Y.M. Xing, L.Y. Yin, Y.N. Zhao, Z.L. Du, H.Q. Tan, X. Qin, W.K. Ho, T.Y. Qiu, Y. G. Li, Construction of the 1D covalent organic Framework/2D g-C₃N₄ heterojunction with high apparent quantum efficiency at 500 nm, ACS Appl. Mater. Interfaces 12 (2020) 51555–51562.

[48] G. Zhou, L.L. Zheng, D.K. Wang, Q.J. Xing, F. Li, P. Ye, X. Xiao, Y. Li, J.P. Zou, A general strategy via chemically covalent combination for constructing heterostructured catalysts with enhanced photocatalytic hydrogen evolution, Chem. Commun. 55 (2019) 4150–4153.

[49] L.B. Wang, B. Cheng, L.Y. Zhang, J.G. Yu, In situ irradiated XPS investigation on S-scheme TiO₂@ZnIn₂S₄ photocatalyst for efficient photocatalytic CO₂ reduction, Small 17 (2021), 2103447.

[50] P. Zhang, Y.K. Li, Y.S. Zhang, R.H. Hou, X.L. Zhang, C. Xue, S.B. Wang, B.C. Zhu, N. Li, G.S. Shao, Photogenerated electron transfer process in heterojunctions: in situ irradiation XPS, Small Methods 4 (2020), 2000214.

[51] J.X. Low, B.Z. Dai, T. Tong, C.J. Jiang, J.G. Yu, In situ irradiated X-Ray photoelectron spectroscopy investigation on a direct Z-scheme TiO₂/CdS composite film photocatalyst, Adv. Mater. 31 (2019), 1802981.

[52] Q.L. Xu, L.Y. Zhang, B. Cheng, J.J. Fan, J.G. Yu, S-scheme heterojunction photocatalyst, Chem 6 (2020) 1543–1559.

[53] Z. Wan, G.K. Zhang, X.Y. Wu, S. Yin, Novel visible-light-driven Z-scheme Bi₁₂GeO₂₀/g-C₃N₄ photocatalyst: oxygen-induced pathway of organic pollutants degradation and proton assisted electron transfer mechanism of Cr(VI) reduction, Appl. Catal. B: Environ. 207 (2017) 17–26.

[54] C. Yang, S.S. Zhang, Y. Huang, K.L. Lv, S. Fang, X.F. Wu, Q. Li, J.J. Fan, Sharply increasing the visible photoreactivity of g-C₃N₄ by breaking the intralayered hydrogen bonds, Appl. Surf. Sci. 505 (2020), 144654.

[55] H. Yang, M. Zhao, J. Zhang, J. Ma, P.Y. Wu, W.L. Liu, L.L. Wen, Noble-metal-free photocatalyst system via BODIPY-based MOFs for highly efficient visible-light-driven H₂ evolution, J. Mater. Chem. A 7 (2019) 20742–20749.

[56] J.J. Liu, B. Cheng, J.G. Yu, A new understanding of the photocatalytic mechanism of the direct Z-scheme g-C₃N₄/TiO₂ heterostructure, Phys. Chem. Chem. Phys. 18 (2016) 31175–31183.

[57] J.C. Wang, T.S. Zhou, Y. Zhang, S. Chen, J. Bai, J.H. Li, H. Zhu, B.X. Zhou, The design of high performance photoanode of CQDs/TiO₂/WO₃ based on DFT alignment of lattice parameter and energy band, and charge distribution, J. Colloid Interface Sci. 600 (2021) 828–883.

[58] J.J. Liu, B. Cheng, J.G. Yu, New understanding on photocatalytic mechanism of direct Z-Scheme g-C$_3$N$_4$/TiO$_2$ heterostructure, Phys. Chem. Chem. Phys. 18 (2016) 31175–31183.

[59] H. Li, B. Yu, Z.C. Zhuang, W.P. Sun, B.H. Jia, T.Y. Ma, A small change in the local atomic environment for a big improvement in single-atom catalysis, J. Mater. Chem. A 9 (2021) 4184.

[60] G. Yan, X.D. Sun, K.L. Zhang, Y. Zhang, H. Li, Y.H. Dou, D. Yuan, H.W. Huang, B. H. Jia, H. Li, T.Y. Ma, Integrating covalent organic framework with transition metal phosphide for noble-metal-free visible-light-driven photocatalytic H$_2$ evolution, Small 18 (2022), 2201340.

[61] V. Gérard, E. Ay, B. Graff, F. Morlet-Savary, C. Galopin, W. Mutilangi, J. Lalevée, Ascorbic acid derivatives as potential substitutes for ascorbic acid to reduce color degradation of drinks containing ascorbic acid and anthocyanins from natural extracts, J. Agric. Food Chem. 67 (2019) 12061–12071.

[62] K. Wang, L.S. Jiang, X.Y. Wu, G.K. Zhang, Vacancy mediated Z-scheme charge transfer in a 2D/2D La$_2$Ti$_2$O$_7$/g-C$_3$N$_4$ nanojunction as a bifunctional photocatalyst for solar-to-energy conversion, J. Mater. Chem. A 8 (2020) 13241–13247.

[63] L.S. Jiang, J. Li, K. Wang, G.K. Zhang, Y. Li, X.Y. Wu, Low boiling point solvent mediated strategy to synthesize functionalized monolayer carbon nitride for superior photocatalytic hydrogen evolution, Appl. Catal. B: Environ. 260 (2020), 118181.

[64] L. Ye, Z.H. Wen, Z.H. Li, H.T. Huang, Hierarchical architectured ternary nanostructures photocatalysts with In(OH)$_3$ nanocube on ZnIn$_2$S$_4$/NiS nanosheets for photocatalytic hydrogen evolution, Sol. RRL 4 (2020), 2000027.

[65] X.M. Xu, L.J. Meng, J. Luo, M. Zhang, Y.T. Wang, Y.X. Dai, C. Sun, Z.Y. Wang, S. G. Yang, H. He, S.B. Wang, Self-assembled ultrathin CoO/Bi quantum dots/defective Bi$_2$MoO$_6$ hollow Z-scheme heterojunction for visible light-driven degradation of diazinon in water matrix: Intermediate toxicity and photocatalytic mechanism, Appl. Catal. B: Environ. 293 (2021), 120231.

[66] M.Y. Ye, Z.H. Zhao, Z.F. Hu, L.Q. Liu, H.M. Ji, Z.R. Shen, T.Y. Ma, 0D/2D heterojunctions of vanadate quantum dots/graphitic carbon nitride nanosheets for enhanced visible-light-driven photocatalysis, Angew. Chem. Int. Ed. 56 (2017) 8407–8411.

[67] P. Zhang, J.Q. Wang, Y. Li, L.S. Jiang, Z.Z. Wang, G.K. Zhang, Non-noble-metallic cocatalyst Ni$_2$P nanoparticles modified graphite-like carbonitride with enhanced photocatalytic hydrogen evolution under visible light irradiation, Acta Phys. Chim. Sin. 37 (2021), 2009102.

[68] H.G. Yu, H.Q. Ma, X.H. Wu, X.F. Wang, J.J. Fan, J.G. Yu, One-step realization of crystallization and cyano-group generation for g-C$_3$N$_4$ photocatalysts with improved H$_2$ production, Sol. RRL 5 (2021), 202000372.

[69] Z.J. Xie, Y.P. Feng, F.L. Wang, D.N. Chen, Q.X. Zhang, Y.Q. Zeng, W.Y. Lv, G.G. Liu, Construction of carbon dots modified MoO$_3$/g-C$_3$N$_4$ Z-scheme photocatalyst with enhanced visible-light photocatalytic activity for the degradation of tetracycline, Appl. Catal. B: Environ. 229 (2018) 96–104.

[70] L. Han, F. Jing, J. Zhang, X.Z. Luo, Y.L. Zhong, K. Wang, S.H. Zang, D.H. Teng, Y. Liu, J. Chen, C. Yang, Y.T. Zhou, Environment friendly and remarkably efficient photocatalytic hydrogen evolution based on metal organic framework derived hexagonal/cubic In$_2$O$_3$ phase-junction, Appl. Catal. B: Environ. 282 (2021), 119602.